Electronic Supplementary Information

Structuring Electrodes via Acoustic-Field-Assisted Particle Patterning for Enhanced Performance of Lithium-Ion Batteries

Yifan Zhang, M Shahriar, Shan Hu*

Department of Mechanical Engineering, Iowa State University, Ames, Iowa 50011, USA

* Corresponding author: shanhu@iastate.edu

Computational analysis of acoustic pressure distribution in the slurry domain

Numerical analysis is applied in this study to investigate the resonant frequency that produces linear pressure distribution inside the domain from each PZT transducer. COMSOL Multiphysics 5.3 is used to simulate the behavior of the acoustic waveform from the PZT transducer to the substrate and the fluid domain. The domain consists of four PZT plates, which are arranged orthogonally along the X and Y axis. The slurry domain that contains active material particles and the aluminum foil is also placed in the X-Y plane. For the simulation, three physics interfaces, including pressure acoustics with frequency sweeping, solid mechanics and electrostatic, have been chosen to define the physical domain for slurry, aluminum foil and the PZT transducer, respectively. Multiphysics couplings have been used to simulate the problem in two study steps. First, we simulated the electrostatics-solid mechanics coupling to analyze the acoustic wave propagation from the PZT to the aluminum foil. The produced surface acoustic wave transmits to the aluminum foil as elastic wave and causes surface deformation. Later, solid mechanics-pressure acoustics coupling is utilized to observe the pattern formation inside the liquid domain which is propagated as leaky wave from the aluminum foil to the slurry. The bottom part of the PZT transducer is assigned to the electrical voltage of 160 V and the top part attached with the aluminum foil is put to ground condition. The "Charge conservation, piezoelectricity" physics converts the applied voltage to the thickness mode vibration that works along Z axis. "Prescribed displacement" boundary condition is applied to the edges of the aluminum foil and the inactive PZT plates are assigned as "Solid hard boundary wall" to form the standing acoustic wave in the electrode slurry. Frequency sweeping was completed from 70 kHz to 140 kHz with the interval of 5 kHz. As a result, 80 kHz frequency was found to produce high-quality acoustic patterns, which was applied in our experiment. Aligned and grid pressure distribution are achieved by activating single and two orthogonally arranged PZTs, respectively, as shown in Fig. S3. The other opposing inactive transducers reflect the incident waveform from the active PZT to create standing surface acoustic wave.

Calculation of lithium-ion diffusion coefficient (D_{Li^+})

Cyclic voltammetry (CV) was performed at scan rate from 0.1 to 0.25 mV/s in the voltage window of 2.5 to 4.2 V for LFP electrode and 1.0 to 2.5 V for LTO electrode. Based on Randles-Sevcik Equation:

$$i_p = 2.69 \times 10^5 n^{3/2} A D_{Li^+}^{1/2} C_{Li^+} \nu^{1/2}$$

where i_p is the peak current, n is the number of electrons transferred in the redox reaction, A is the area of electrode, D_{Li^+} is the diffusion coefficient of lithium-ion, C_{Li^+} is the change of concentration of lithium-ion, ν is the scan rate, the peak current (i_p) is linearly related to the square root of scan rate ($\nu^{1/2}$). Fig. 5c and 5f were plotted fitting the peak current and square root of scan rate. As n, A and C_{Li^+} are all constants, coefficient of lithium-ion diffusion is calculated by the slope of fitted line for each electrode.

Galvanostatic intermittent titration technique (GITT) was applied to compare the diffusion among the electrodes. For both LFP and LTO electrode, charge and discharge pulse was set as 30 minutes at the rate of 0.1 C, followed by 1 hour of relaxation before the next current pulse. To calculate the diffusion coefficient based on the GITT profile, diffusion coefficient of lithium-ions D_{Li^+} is expressed by:

$$D_{Li^+} = \frac{4}{\pi\tau}\left(\frac{nV_m}{A}\right)^2\left(\frac{\Delta E_s}{\Delta E_\tau}\right)^2$$

in which τ is the time of current pulse, n is the moles of active material, V_m is the molar volume, A is the area of the electrode, ΔE_s is the change of steady-state voltage, and ΔE_τ is the voltage change during charge/discharge pulse. Detailed acquisition of the parameters is shown in Fig. S14.

Furthermore, electrochemical impedance spectroscopy (EIS) was measured to obtain the Nyquist plot. According to the semi-infinite diffusion model, the Warburg impedance (W) is expressed as:

$$W = \sigma\omega^{-1/2}(1 - j)$$

where σ is the Warburg coefficient and ω is the angular frequency. By fitting the plot of the Warburg impedance (W) against the inverse square root of the angular frequency ($\omega^{-1/2}$) at low frequency region, the slope of fitted line indicates the Warburg coefficient (σ). As σ is inversely proportional to the square root of lithium-ion diffusion coefficient (D_{Li^+}), which is expressed as:

$$\sigma = \frac{RT}{\sqrt{2}An^2F^2CD_{Li^+}^{1/2}}$$

where R is ideal gas constant (8.314 J mol^{-1} K^{-1}), T is the temperature, A is the area of electrode surface, n is the number of electrons involved in the redox reaction, F is Faraday constant (96485 C mol^{-1}), C is the molar concentration of lithium ions, D_{Li^+} can be calculated with the σ obtained from the slope of fitted line shown in Fig. S15c.

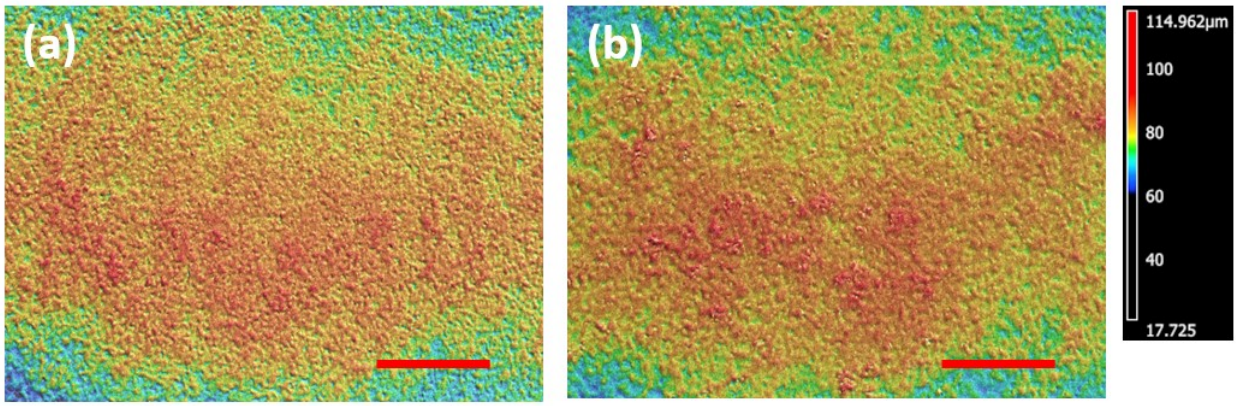

Fig. S1 Confocal microscopy images of (a) CC-LFP and (b) CC-LTO (scale bar: 500-µm).

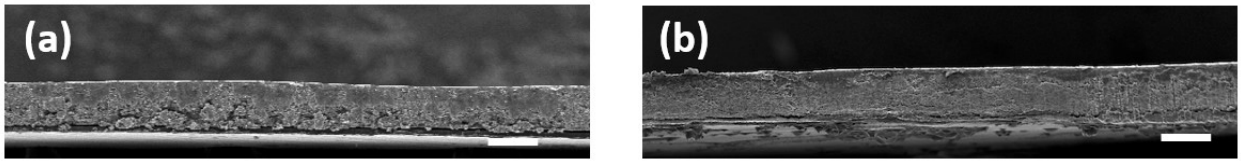

Fig. S2 SEM images of (a) CC-LFP and (b) CC-LTO (scale bar: 100-μm).

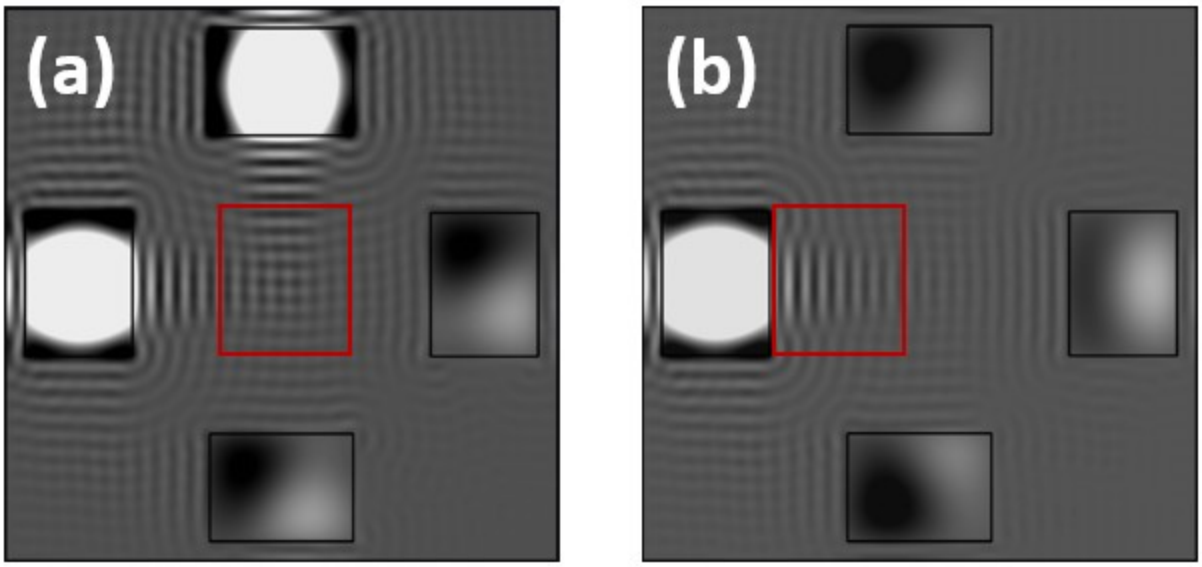

Fig. S3 Acoustic pressure distribution in the slurry domain with 80 kHz as applied frequency by activating (a) orthogonally arranged two PZT plates to form grid pattern and (b) a single PZT plate to generate the line pattern. The marked regions in both figures represent the areas selected to acquire electrodes for coin-cell assembly.

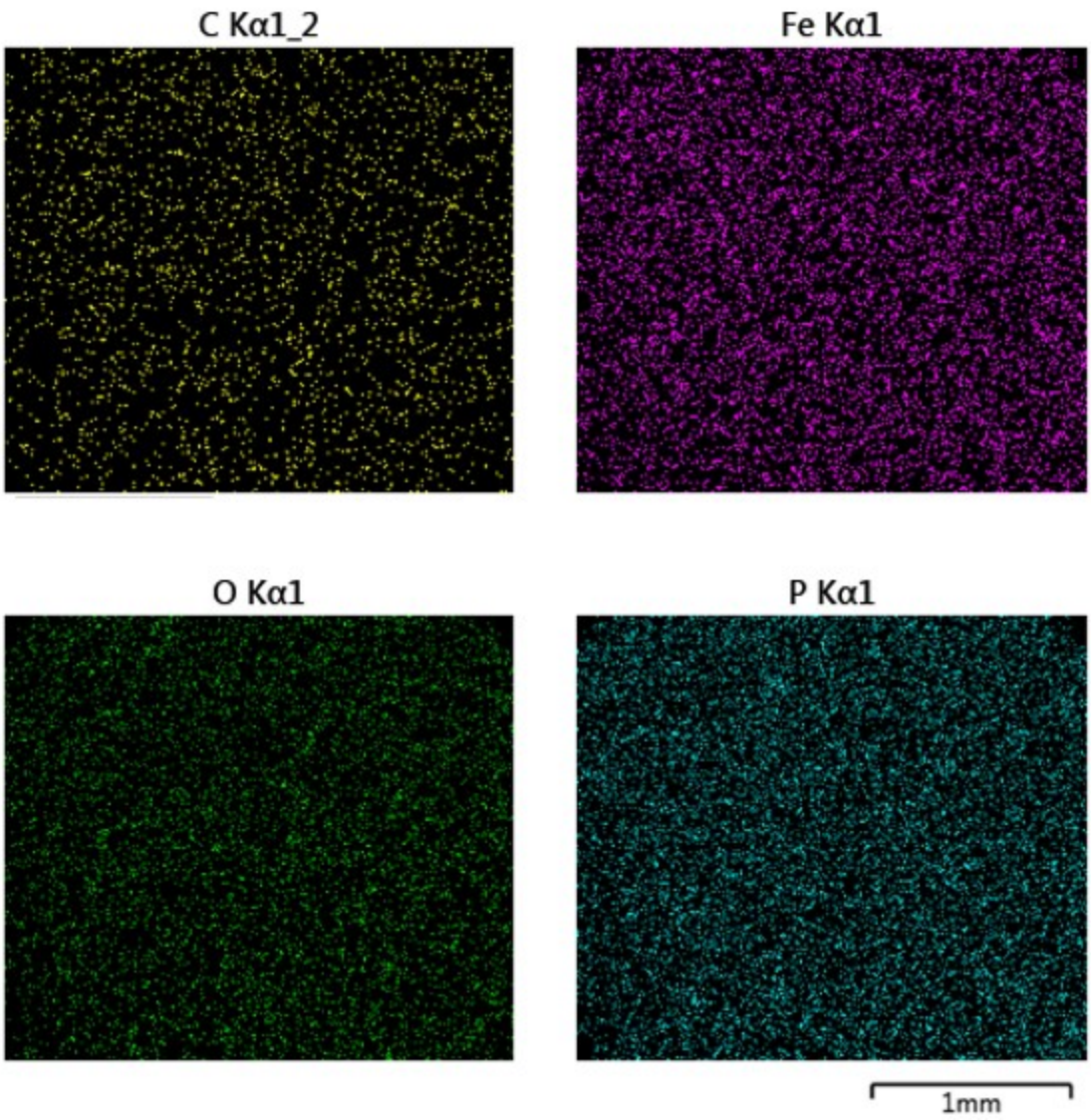

Fig. S4 EDS mapping of top surface of G-LFP.

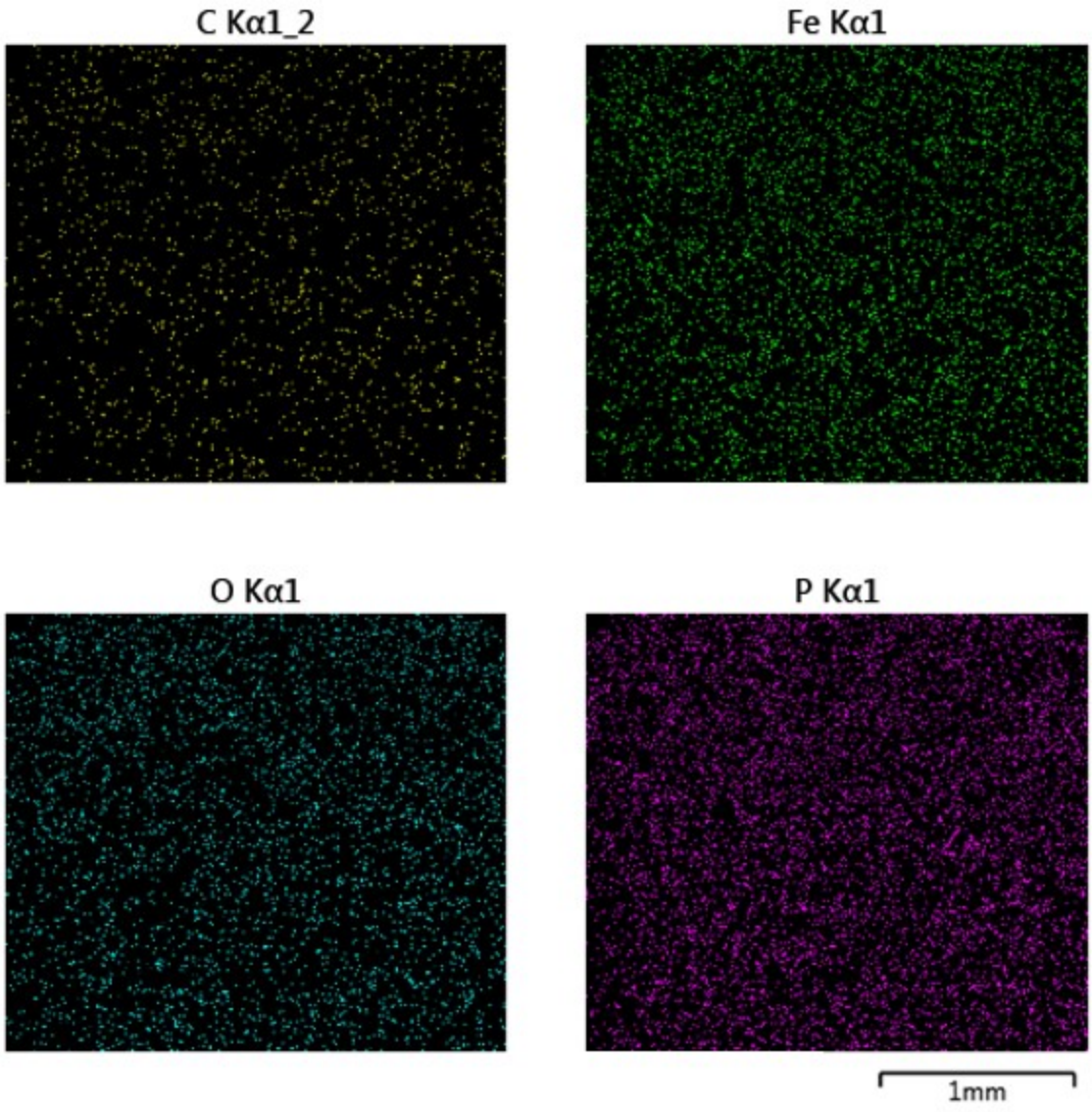

Fig. S5 EDS mapping of top surface of L-LFP.

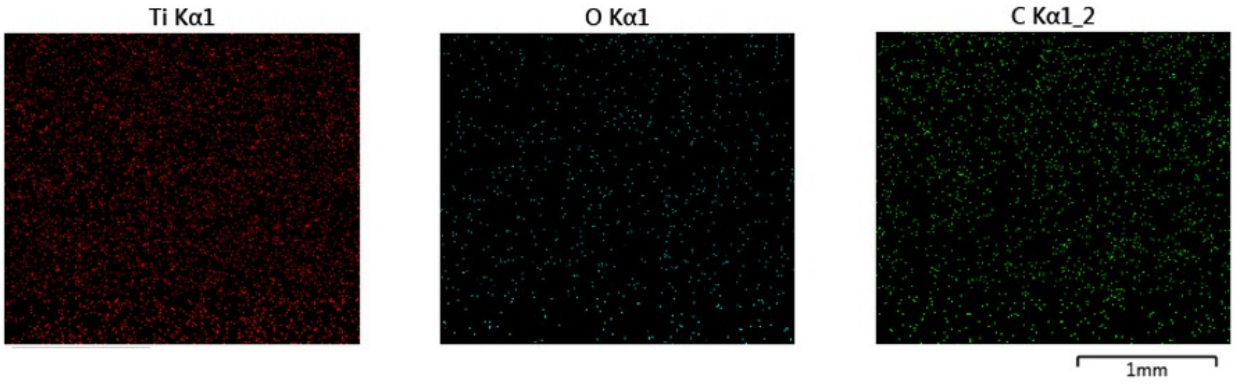

Fig. S6 EDS mapping of top surface of G-LTO.

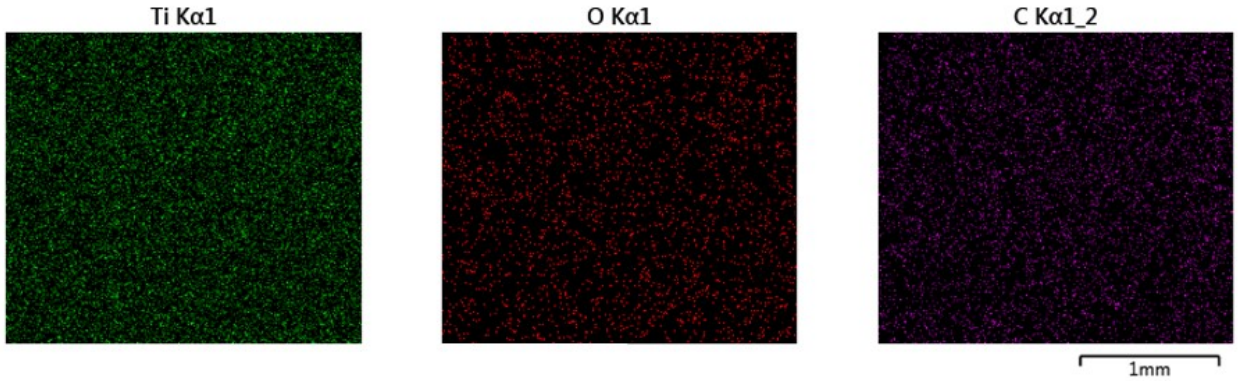

Fig. S7 EDS mapping of top surface of L-LTO.

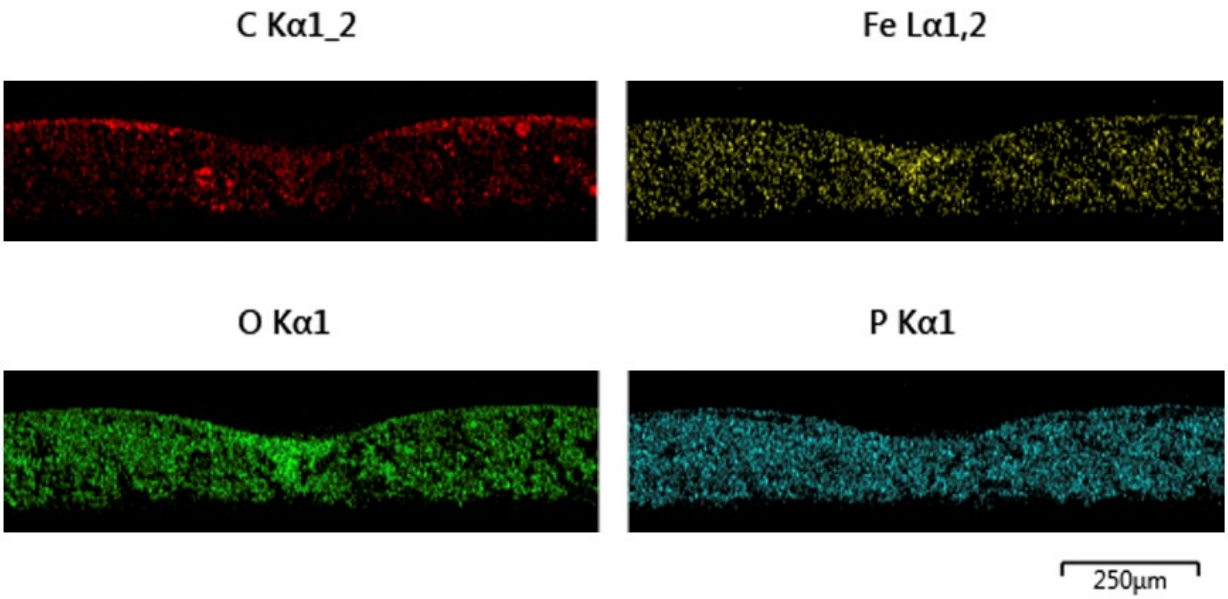

Fig. S8 EDS mapping of cross-sectional area of G-LFP.

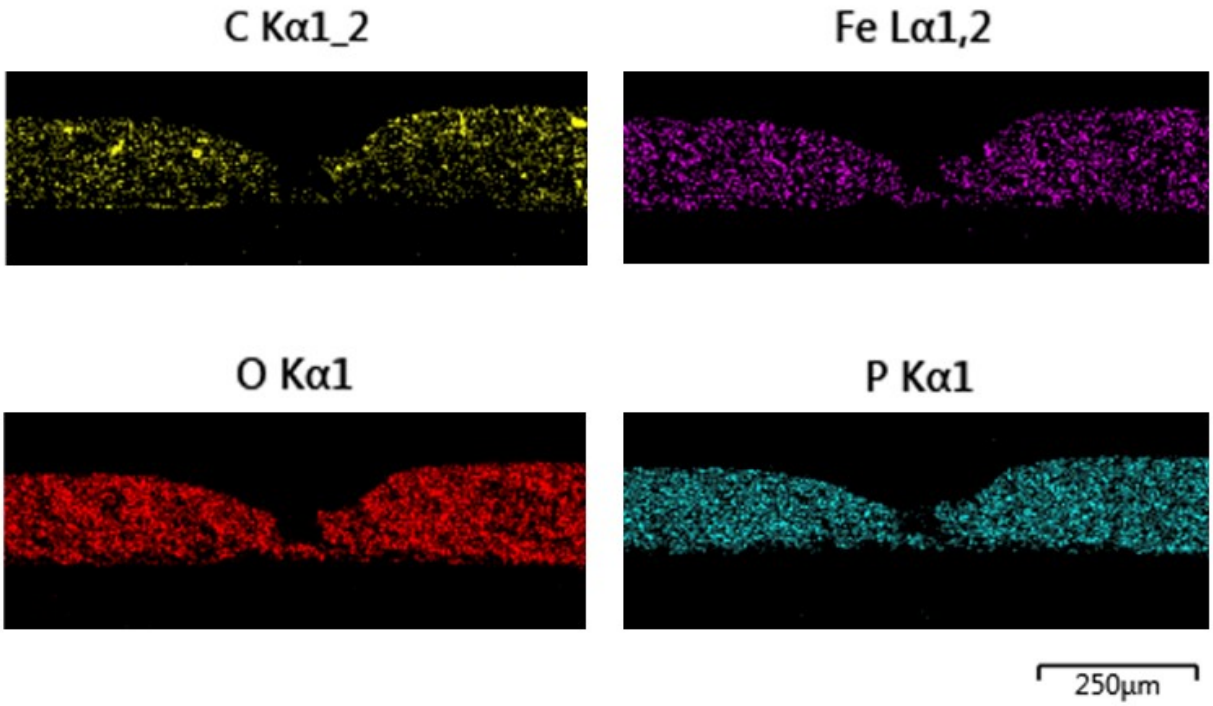

Fig. S9 EDS mapping of cross-sectional area of L-LFP.

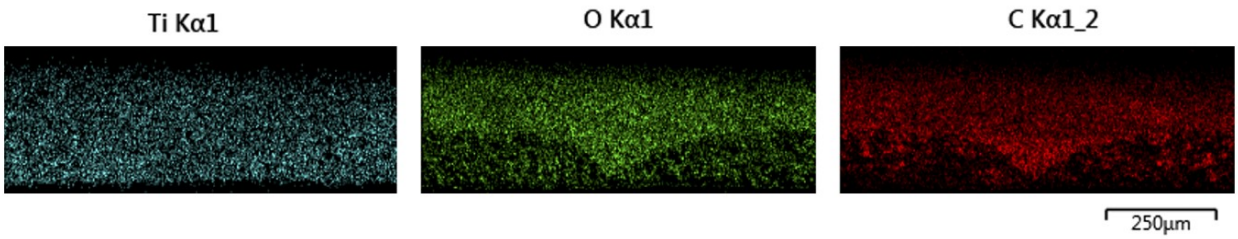

Fig. S10 EDS mapping of cross-sectional area of G-LTO.

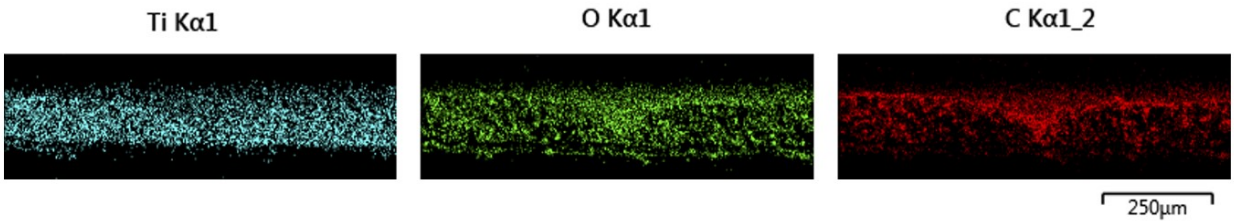

Fig. S11 EDS mapping of cross-sectional area of L-LTO.

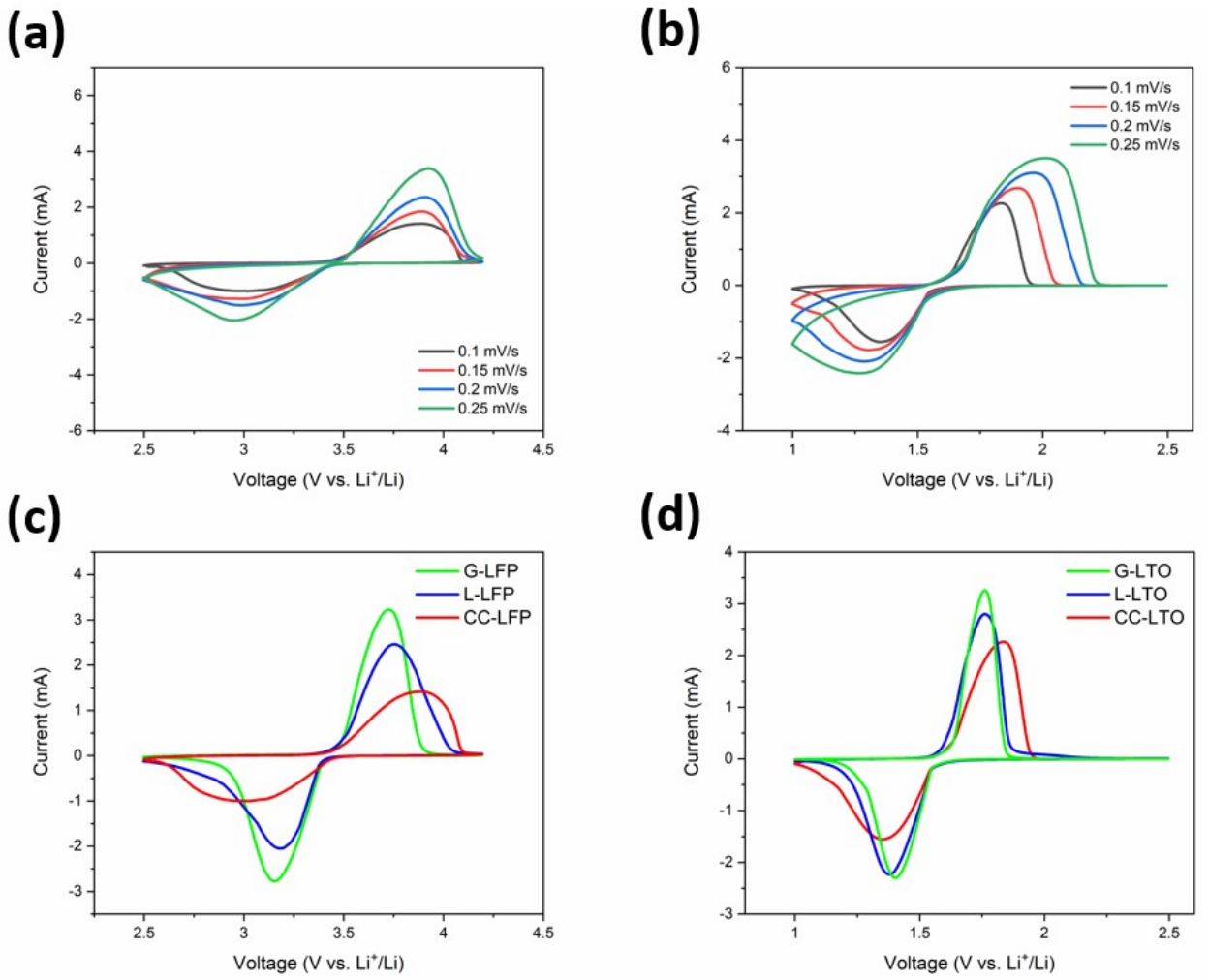

Fig. S12 Cyclic voltammograms of (a) CC-LFP and (b) CC-LTO electrodes at scan rate of 0.1, 0.15, 0.2 and 0.25 mV/s. Comparison of cyclic voltammograms acoustically patterned electrodes and conventionally fabricated electrode at scan rate of 0.1 mV/s: (c) LFP electrodes, (d) LTO electrodes.

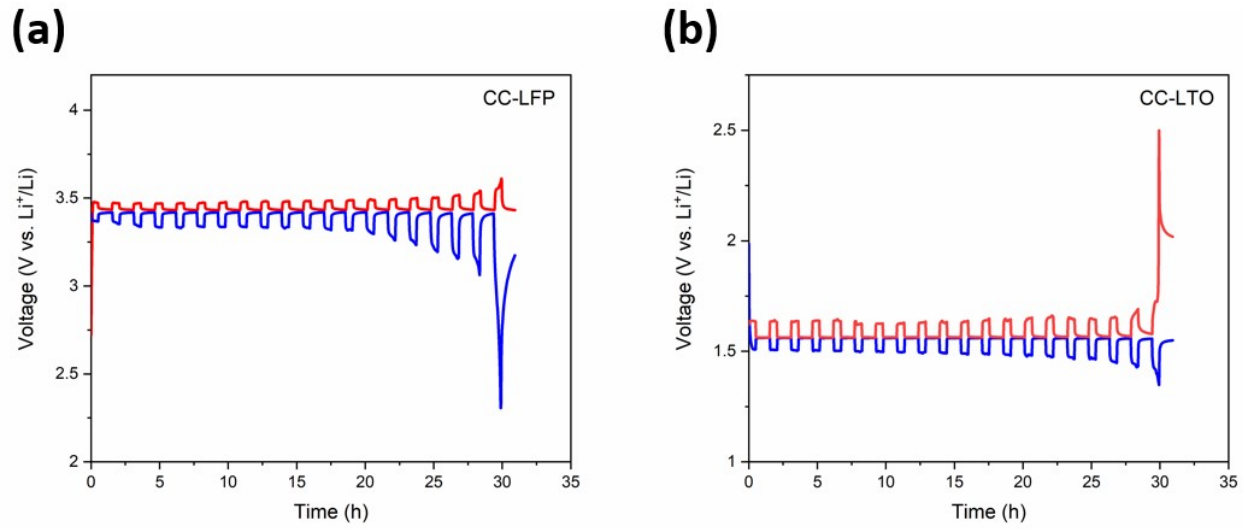

Fig. S13 GITT profiles of (a) CC-LFP and (b) CC-LTO.

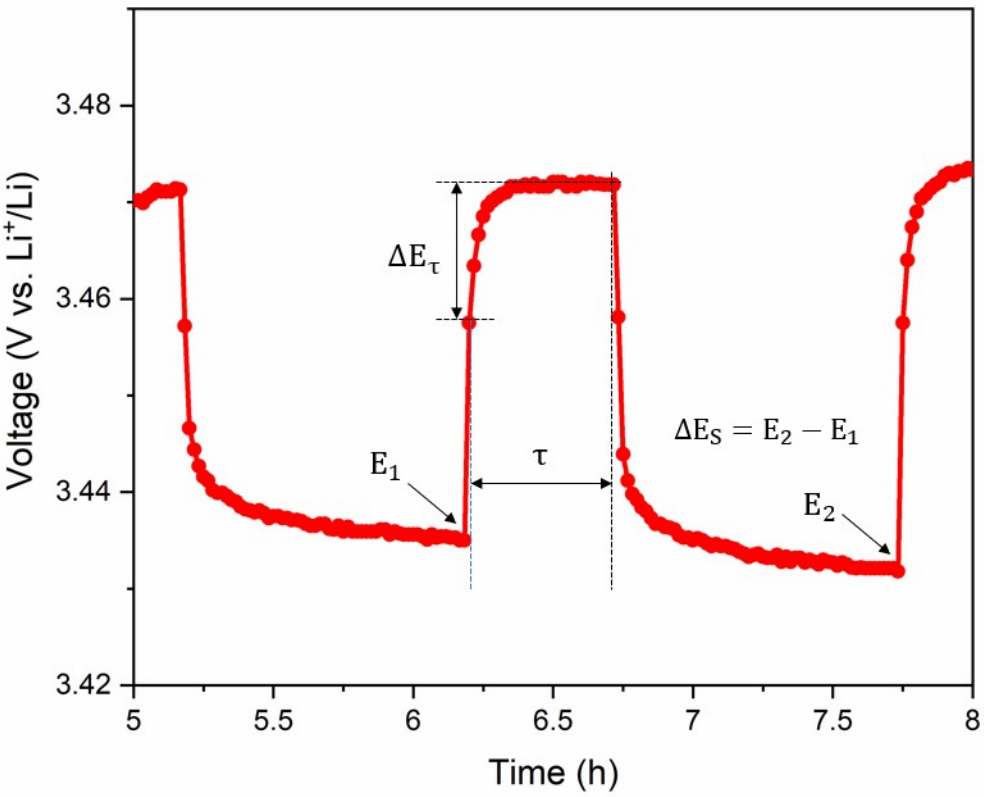

Fig. S14 Example charging step of G-LFP with symbolized parameters in calculation.

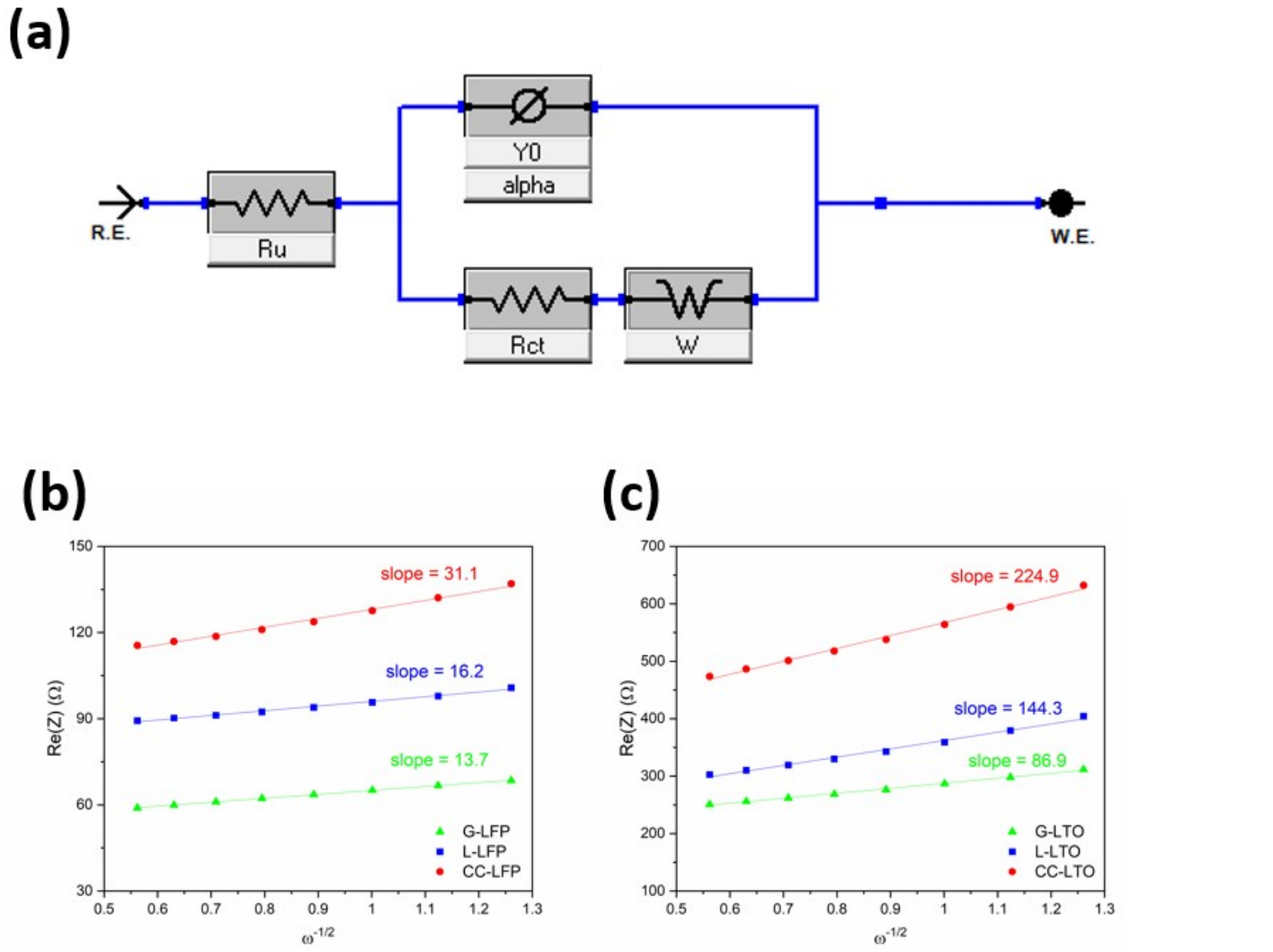

Fig. S15 (a) Equivalent circuit for EIS analysis. Fitted line of low-frequency region of EIS measurement versus inverse square root of the angular frequency ($\omega^{-1/2}$): (b) LFP electrodes; (c) LTO electrodes.

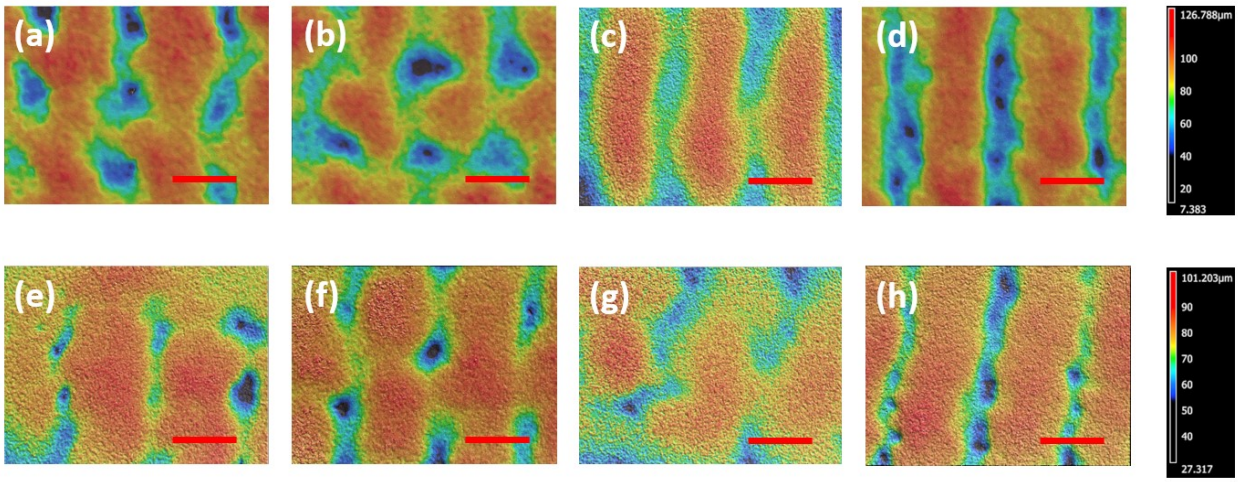

Fig. S16 Confocal microscopy images of the top surface of acoustic-field-assisted patterned electrodes without calendering: (a) G-LFP, (b) G-LTO, (c) L-LFP and (d) L-LTO and the corresponding electrode after calendering into thickness around 100-µm (e-h) (scale bar: 500-µm).

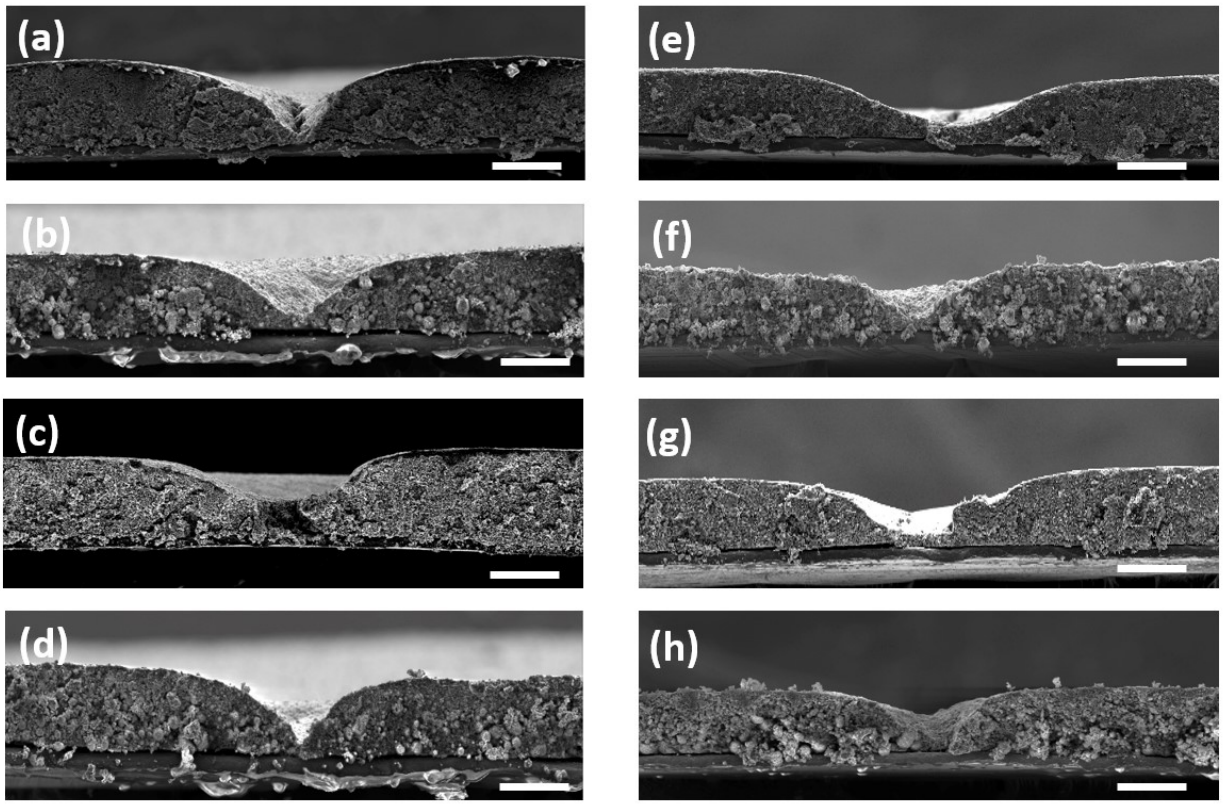

Fig. S17 SEM images of cross-sectional area of acoustic-field-assisted patterned electrodes without calendering: (a) G-LFP, (b) G-LTO, (c) L-LFP and (d) L-LTO and the corresponding electrode after calendering into thickness around 100-μm (e-h) (scale bar: 100-μm).

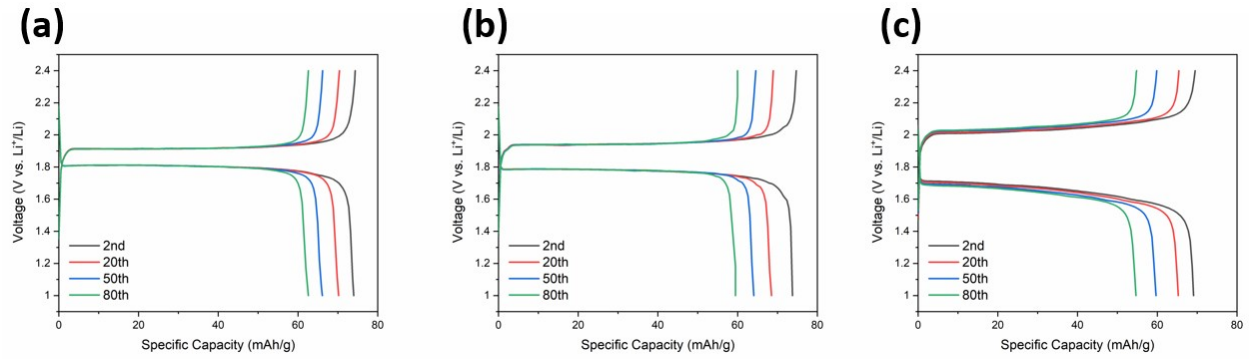

Fig. S18 Charge and discharge profiles of 2nd, 20th, 50th and 80th cycle of (a) G-Cell, (b) L-Cell and (c) CC-Cell at rate of C/3.

Table S1 Fitted line slope of peak current (i_p) against square root of scan rate ($\nu^{1/2}$) in Fig. 5c and 5f with the calculated lithium-ion diffusion coefficient.

Electrode	**Charge**	$D_{Li^+,\ Charge}$ **($cm^2\ s^{-1}$)**	**Discharge**	$D_{Li^+,\ Discharge}$ **($cm^2\ s^{-1}$)**
G-LFP	421.8	4.73×10^{-9}	321.5	2.75×10^{-9}
L-LFP	397.6	4.20×10^{-9}	247.5	1.63×10^{-9}
CC-LFP	289.0	2.22×10^{-9}	149.6	5.95×10^{-10}
G-LTO	297.0	8.72×10^{-11}	221.4	4.84×10^{-11}
L-LTO	269.4	7.17×10^{-11}	201.7	4.02×10^{-11}
CC-LTO	213.9	4.52×10^{-11}	148.2	2.17×10^{-11}

Table S2 Lithium-ion diffusion coefficients obtained from GITT profiles.

Electrode	D_{Li^+} (cm² s⁻¹)
G-LFP	3.31×10^{-9}
L-LFP	2.79×10^{-9}
CC-LFP	1.51×10^{-9}
G-LTO	5.53×10^{-11}
L-LTO	3.13×10^{-11}
CC-LTO	1.00×10^{-11}

Table S3 Key parameters of Nyquist plots and calculated diffusion coefficient of lithium ions for each electrode.

Electrode	R_u (Ω)	R_{ct} (Ω)	D_{Li^+} ($cm^2\ s^{-1}$)
G-LFP	3.926	50.7	1.89×10^{-10}
L-LFP	3.356	90.6	1.34×10^{-10}
CC-LFP	6.760	120.1	3.67×10^{-11}
G-LTO	2.043	226.3	4.70×10^{-12}
L-LTO	3.791	312.0	1.70×10^{-12}
CC-LTO	3.290	446.3	7.01×10^{-13}

Table S4 Volumetric energy density (Wh/L) of LFP and LTO electrodes at various C-rates.

Electrode	0.1 C	0.2 C	0.5 C	1 C	2 C	3 C	5 C
G-LFP	739.14	722.17	695.85	653.54	574.37	488.26	241.44
L-LFP	718.17	702.35	651.75	589.81	474.77	394.71	140.51
CC-LFP	673.65	649.11	600.20	554.63	395.03	205.68	18.17
G-LTO	353.61	347.37	338.65	324.69	294.02	257.11	191.74
L-LTO	346.60	344.04	329.26	300.12	238.80	167.23	50.16
CC-LTO	329.11	326.11	320.60	273.37	97.62	43.55	5.63